



# Compressive creep of SiC whisker/Ti<sub>3</sub>SiC<sub>2</sub> composites at high temperature in air

Apurv Dash<sup>1,2</sup>  | Jürgen Malzbender<sup>1</sup> | Khushbu Dash<sup>3</sup> | Marcin Rasinski<sup>1</sup> | Robert Vaßen<sup>1</sup> | Olivier Guillon<sup>1,2,4</sup> | Jesus Gonzalez-Julian<sup>1,2</sup> 

<sup>1</sup>Forschungszentrum Jülich GmbH, Institute of Energy and Climate Research, Jülich, Germany

<sup>2</sup>Department of Ceramics and Refractory Materials, Institute for Mineral Engineering (GHI), RWTH Aachen University, Aachen, Germany

<sup>3</sup>Metallurgical and Materials engineering, Indian Institute of Technology Madras, Chennai, India

<sup>4</sup>Jülich Aachen Research Alliance, JARA-Energy, Jülich, Germany

## Correspondence

Apurv Dash, Forschungszentrum Jülich GmbH, Institute of Energy and Climate Research, Jülich-52425, Germany.  
Email: a.dash@fz-juelich.de

## Funding information

Bundesministerium für Bildung und Forschung, Grant/Award Number: 03SF0534

## Abstract

The compressive creep of a SiC whisker (SiC<sub>w</sub>) reinforced Ti<sub>3</sub>SiC<sub>2</sub> MAX phase-based ceramic matrix composites (CMCs) was studied in the temperature range 1100–1300°C in air for a stress range 20–120 MPa. Ti<sub>3</sub>SiC<sub>2</sub> containing 0, 10, and 20 vol% of SiC<sub>w</sub> was sintered by spark plasma sintering (SPS) for subsequent creep tests. The creep rate of Ti<sub>3</sub>SiC<sub>2</sub> decreased by around two orders of magnitude with every additional 10 vol% of SiC<sub>w</sub>. The main creep mechanisms of monolithic Ti<sub>3</sub>SiC<sub>2</sub> and the 10% CMCs appeared to be the same, whereas for the 20% material, a different mechanism is indicated by changes in stress exponents. The creep rates of 20% composites tend to converge to that of 10% at higher stress. Viscoplastic and viscoelastic creep is believed to be the deformation mechanism for the CMCs, whereas monolithic Ti<sub>3</sub>SiC<sub>2</sub> might have undergone only dislocation-based deformation. The rate controlling creep is believed to be dislocation based for all the materials which is also supported by similar activation energies in the range 650–700 kJ/mol.

## KEYWORDS

CMC, compression, creep, MAX phases, SiC whiskers, Ti<sub>3</sub>SiC<sub>2</sub>

## 1 | INTRODUCTION

MAX phases are a class of ternary carbides or nitride ceramic materials characterized by nanolaminated layers.<sup>1</sup> The uniqueness of MAX phases lies in the fact that they can be easily machined and they are categorized as ceramic materials with the advantage of low density unlike metals and good damage tolerance unlike other conventional ceramics.<sup>2</sup> Ti<sub>3</sub>SiC<sub>2</sub> is the most studied MAX phase because of its superior mechanical properties, both at room and high temperature, compared to other MAX phases.<sup>3–6</sup> Since Ti<sub>3</sub>SiC<sub>2</sub> is stable at high temperature (<1000°C in air, <1600°C in

vacuum), it is a potential candidate for applications where thermomechanical stability is required such as parts of the turbo jet engines.<sup>7</sup>

The availability of Ti<sub>3</sub>SiC<sub>2</sub> powders has limited the investigation on ceramic matrix composites (CMCs) with Ti<sub>3</sub>SiC<sub>2</sub> or any other MAX phase matrix, however, Lenz et al fabricated C<sub>f</sub>/Ti<sub>3</sub>SiC<sub>2</sub> composite by reactive melt infiltration of Si into C<sub>f</sub> preforms impregnated with a mix of phenolic resin and TiC particles.<sup>8</sup> Mu et al reported an increase in flexural strength with the addition of only 9 wt% of Ti<sub>3</sub>SiC<sub>2</sub> particles as filler in SiC<sub>f</sub>/SiC composites.<sup>9</sup> Yin et al manufactured C-SiC-Ti<sub>3</sub>SiC<sub>2</sub> hybrid composites by the combination of TiC

This is an open access article under the terms of the Creative Commons Attribution License, which permits use, distribution and reproduction in any medium, provided the original work is properly cited.

© 2020 The Authors. *Journal of the American Ceramic Society* published by Wiley Periodicals LLC on behalf of American Ceramic Society (ACERS) The Authors. *Journal of the American Ceramic Society* published by Wiley Periodicals LLC on behalf of American Ceramic Society (ACERS)

slurry and liquid silicon infiltration.<sup>10</sup> The final composite had 4 vol% of  $\text{Ti}_3\text{SiC}_2$  which resulted in the improvement of both flexural strength and fracture toughness. Lagos et al fabricated  $\text{Ti}_3\text{SiC}_2$ -based CMCs by densification with spark plasma sintering (SPS) of mixed chopped carbon fiber and  $\text{Ti}_3\text{SiC}_2$  powder.<sup>11</sup> There was an interfacial reaction between carbon fiber and  $\text{Ti}_3\text{SiC}_2$  which might lead to the degradation of mechanical properties.

It was reported by Spencer et al that  $\text{Ti}_3\text{SiC}_2$  does not react with SiC fibers even at higher temperatures of 1550°C and, hence,  $\text{SiC}_w$  was selected as the reinforcement in the present work.<sup>12</sup> The inertness of SiC with respect to  $\text{Ti}_3\text{SiC}_2$  provides the possibility of  $\text{SiC}_w/\text{Ti}_3\text{SiC}_2$  CMCs. Gonzalez et al fabricated SiC fiber containing CMCs with  $\text{Cr}_2\text{AlC}$  and  $\text{Ti}_2\text{AlC}$  MAX phases as the matrix.<sup>13,14</sup> A reaction was observed in the interface of  $\text{Ti}_2\text{AlC}$  and SiC fiber, whereas no reaction was observed in  $\text{Cr}_2\text{AlC}$ -SiC fiber interface. Considering the better creep resistance of  $\text{Ti}_3\text{SiC}_2$  reported in literature as compared to other MAX phases,  $\text{Ti}_3\text{SiC}_2$  was used as the matrix in the present study. Moreover, SiC particles were also used to improve the tribological properties of  $\text{Ti}_3\text{SiC}_2$ .<sup>15</sup> Wan et al improved the fracture toughness of  $\text{Ti}_3\text{SiC}_2$  by the addition of 30 vol% of SiC particles.<sup>16</sup> Zhou et al and Li et al used SiC reinforcement to improve the oxidation resistance of  $\text{Ti}_3\text{SiC}_2$  at high temperature and these results are indicative of better oxidation resistance of the composites fabricated in the present work.<sup>17,18</sup> Recently, we also explored the effect of short SiC fibers 1 mm on the creep behavior of  $\text{Ti}_3\text{SiC}_2$ .<sup>19</sup>

The evaluation of mechanical properties of MAX phase-based composites is majorly done at room temperature.<sup>20,21</sup> The high-temperature mechanical property evaluation of short-fiber reinforced MAX phase has not been reported up to now and, hence, this work presents the evaluation of compressive creep of SiC whisker ( $\text{SiC}_w$ ) reinforced  $\text{Ti}_3\text{SiC}_2$  MAX phase. For the usage of components at a high temperature for a prolonged time under a constant stress they should have good creep resistance at the operation temperature. Creep resistance is an important aspect, which needs to be considered for thermomechanical applications.<sup>22</sup> The mechanical properties like flexural strength (room and high temperature)<sup>20</sup> and tribological behavior<sup>23</sup> of MAX phase are well documented and reported, however, creep investigations of MAX phase materials are very limited.<sup>4,5,24-26</sup> Radovic et al measured the tensile creep of both fine- and coarse-grained  $\text{Ti}_3\text{SiC}_2$  in the temperature range 1000-1200°C. The coarse-grained  $\text{Ti}_3\text{SiC}_2$  had higher creep rate since large grains are more prone to delamination and kink-band formation thereby absorbing the stresses. The activation energies (~460 kJ/mol) and stress exponent (1.5-2) for creep were similar for both coarse- and fine-grained  $\text{Ti}_3\text{SiC}_2$  and dislocation creep was the proposed dominant mechanism.<sup>5,24</sup> The overall creep response was attributed to the formation and relaxation

of internal stresses. Zhen et al investigated the creep response of fine- and coarse-grained  $\text{Ti}_3\text{SiC}_2$  in compressive mode.<sup>4</sup> Although the creep rate was found to be a magnitude lower than that in the tension mode, the creep mechanism was attributed to dislocation with the possibility of subcritical crack growth and grain boundary sliding (GBS) because of similar stress exponent values as that in tension mode.

Since the deformation of  $\text{Ti}_3\text{SiC}_2$  is only based on basal slip both at room and high temperature, the understanding of the creep behavior of  $\text{Ti}_3\text{SiC}_2$  reinforced with  $\text{SiC}_w$  will provide more insights about thermomechanical properties of MAX phase-based CMCs, hence, being the focus of the current work. In the present work, we have used  $\text{SiC}_w$  as the reinforcing phase in  $\text{Ti}_3\text{SiC}_2$  MAX phase matrix. The motivation of using  $\text{Ti}_3\text{SiC}_2$  as the matrix material is the pseudoductility of the same provided by a combination of mechanisms like kinking, shear band, and basal slip.<sup>27</sup>

## 2 | EXPERIMENTAL PROCEDURE

$\text{Ti}_3\text{SiC}_2$  MAX phase was synthesized by starting with elemental reactants (Ti, Si, Al, and C) and following a process named as molten shielded salt synthesis in air. The details of the synthesis process are given elsewhere.<sup>28</sup> Briefly, the elemental precursors were mixed in stoichiometric ratio with equal weight of KBr and further encapsulated with KBr to form a gas-tight cladding. Then, the pellets were placed in a KBr salt bed for high-temperature processing in air without the need of protective atmosphere. The molten KBr at high temperature serves as a barrier between the material and ambient atmosphere. The synthesis of  $\text{Ti}_3\text{SiC}_2$  was done at 1250°C for 1 hour, followed by cooling and washing the KBr content to obtain free flowing powder. The resultant powder was agglomerated hence it was milled on a roller bench in a slurry form for 24 hours with zirconia balls (3 mm diameter) in ethanol medium to break the loosely bound agglomerates. The milled slurry was dried in a rotary evaporator at 60°C to obtain soft agglomerates. The dried powder was then passed through a 300  $\mu\text{m}$  sieve to obtain homogeneously agglomerated particles of  $\text{Ti}_3\text{SiC}_2$  MAX phase.

As-received  $\beta\text{-SiC}_w$  (length: 10  $\mu\text{m}$ , diameter of 1  $\mu\text{m}$ ; Haydale Technologies) were processed to remove the metal catalyst used for the growth of whiskers. Ten grams of  $\text{SiC}_w$  was mixed with 100 mL of 0.1 mol/L  $\text{HNO}_3$  with continuous magnetic stirring at a temperature of 70°C for 1 hour. The suspension of  $\text{SiC}_w$  in diluted  $\text{HNO}_3$  was filtered and repeatedly washed with de-ionized water to confirm the removal of added  $\text{HNO}_3$ . Acid-treated  $\text{SiC}_w$  was finally rinsed with ethanol and dried at 60°C to avoid agglomeration. The characterization of starting materials for the fabrication of CMC was done in a scanning electron microscope (SEM; Zeiss Ultra55).

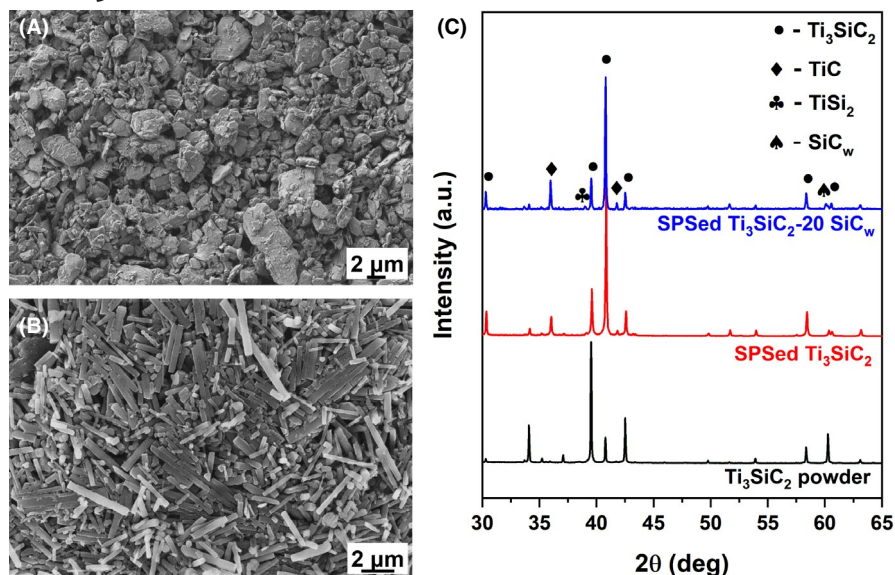


**FIGURE 1** Scanning electron microscopy of synthesized  $\text{Ti}_3\text{SiC}_2$  powder (A), as-received SiC whiskers (B), and X-ray diffraction of initial powder and sintered  $\text{Ti}_3\text{SiC}_2$  MAX phase composites (C) [Color figure can be viewed at [wileyonlinelibrary.com](http://wileyonlinelibrary.com)]

The synthesized  $\text{Ti}_3\text{SiC}_2$  was mixed with 10 and 20 vol% of  $\text{SiC}_w$  in ethanol with high shear mixer in an ultrasonic bath for 1 hour immediately followed by drying in a rotary evaporator to avoid segregation of phases due to density differences. The dried powder mix of  $\text{Ti}_3\text{SiC}_2$  and  $\text{SiC}_w$  was loaded into a graphite die (inner diameter of 20 mm) with a graphite foil. The weight of powder was so calculated to have a sintered block with 20 mm as diameter and 10 mm as height upon full densification by SPS (HPD5; FCT System). The graphite die with the powder was heated at a rate of  $100^\circ\text{C}/\text{min}$  with a holding time of 35 minutes and 80 MPa at the peak temperature of  $1250^\circ\text{C}$  followed by rapid cooling. Additionally, a blank specimen based on monolithic  $\text{Ti}_3\text{SiC}_2$  was sintered under the same conditions to be compared with the composites. The density was measured by Archimedes method of water displacement. The sintered dense blocks were sand blasted to remove the graphite foil used to separate the contact between MAX phase and graphite die wall. Further the sintered block was ground plane-parallel and cylinders with a diameter of 5 mm and a height of 10 mm were obtained by electrodischarge machining. Three different blocks were sintered with monolithic  $\text{Ti}_3\text{SiC}_2$ , and 10 and 20 vol% of  $\text{SiC}_w$  which is referred to as TSC, TSC-10 $\text{SiC}_w$ , and TSC-20 $\text{SiC}_w$ , respectively. The fabricated CMCs were analyzed for identifying crystalline phases by X-ray diffraction (XRD; D4 Bruker). The quantitative analysis from XRD data was obtained by Rietveld analysis using Topas software. The microstructure of the composites was observed in a SEM (Zeiss Ultra55).

The creep tests followed testing procedures reported in the work by, for example, Stournari et al.<sup>29</sup> The creep testing was done in air at temperatures of 1100, 1200, and  $1300^\circ\text{C}$  using constant loads corresponding to stress levels of 20–120 MPa. The creep data were not analyzed below  $1100^\circ\text{C}$  since the deformation was too small (1  $\mu\text{m}/\text{d}$ ) and dominated by primary

creep. The samples were heated to the test temperature at 5 K/min and a holding time of 1 hour was allowed for equilibrium to be achieved between the furnace and sample temperature before the application of constant load by an electromechanical machine (INSTRON 1362). The creep tests were performed for a specific temperature and stress level until a deformation of 100  $\mu\text{m}$  after which the tests were aborted. The deformation was measured by a linear variable differential transformer (Solartron Metrology). The same sample was subjected to a higher temperature and a higher stress after the deformation at a corresponding lower temperature and lower stress exceeded 100  $\mu\text{m}$ . A total of 12 combinations of temperature and stress were used to measure the creep deformation on the single cylindrical specimen. The creep at lower temperatures ( $1100$ – $1200^\circ\text{C}$ ) might affect the creep at  $1300^\circ\text{C}$ , hence creep measurements were in addition carried out on a pristine specimen by directly applying a higher load at a higher temperature (eg,  $1200^\circ\text{C}/80$  MPa). The values for the total deformation over time and the minimum creep rate obtained in these tests were in agreement with the creep testing done by sequential increase in temperature and stress on the same sample, hence, verifying the procedure.

The samples before and after creep tests were ground and polished in both parallel and perpendicular direction of the applied load for electron backscattered diffraction (EBSD, Aztec 2.4; Oxford Instruments) analysis. To avoid the usage of highly corrosive hydrofluoric acid (HF) for etching the grain boundaries, band contrast from kikuchi patterns was used for the reconstruction of an image which is a representation of the microstructure.

Samples for transmission electron microscopy (TEM) were prepared by Focused Ion Beam (FIB, Zeiss Crossbeam 540) equipped with scanning transmission electron microscopy detector (4-Channel aSTEM Detector) for STEM analysis as well as electron backscatter diffraction detector for



EBSD analysis on TEM lamellas (transmission kikuchi diffraction). The lamella was obtained from the center of the crept sample as it is believed to have undergone maximum deformation during creep. The lamella was characterized by TEM (FEI Tecnai G<sup>2</sup> 20S-TWIN).

### 3 | RESULTS

The synthesized  $\text{Ti}_3\text{SiC}_2$  powder (Figure 1A) exhibits a platelet-like morphology with a mean particle size ( $d_{50}$ ) of 6  $\mu\text{m}$ . The  $\text{SiC}_w$  (Figure 1B) particles have a diameter of 0.5  $\mu\text{m}$  and an approximate length of 5  $\mu\text{m}$ . Figure 1C shows the XRD of  $\text{Ti}_3\text{SiC}_2$  powder, SPS-sintered  $\text{Ti}_3\text{SiC}_2$ , and 20 vol%  $\text{SiC}_w$ -reinforced  $\text{Ti}_3\text{SiC}_2$ . TSC-10 $\text{SiC}_w$  is not shown because it is same as that of TSC-20 $\text{SiC}_w$ . The XRD peaks correspond to  $\text{Ti}_3\text{SiC}_2$ ,  $\text{SiC}_w$ , and other phases like TiC and  $\text{TiSi}_2$ . There is no direct implication of any interfacial chemical reaction between  $\text{SiC}_w$  and  $\text{Ti}_3\text{SiC}_2$  that could have compromised the structural integrity of the final CMC.

Although the starting  $\text{Ti}_3\text{SiC}_2$  powder presented only 3 wt% of TiC and 1 wt% of  $\text{Al}_2\text{O}_3$ , the sintered  $\text{Ti}_3\text{SiC}_2$  has a higher content of TiC (8.8 wt%) and  $\text{Al}_2\text{O}_3$  (4.6 wt%). The higher content of TiC might have resulted from the thermal decomposition of  $\text{Ti}_3\text{SiC}_2$  during sintering, whereas the increase in the  $\text{Al}_2\text{O}_3$  content from 1 to 4.6 wt% after sintering can be related to the crystallization of amorphous aluminum hydroxide which could not be detected by XRD in the powder stage. The referred aluminum hydroxide might have formed due to the reaction of unreacted Al with water during the washing step after the molten salt-based synthesis process.<sup>28,30</sup> The proposed mechanism of decomposition is by deintercalation of Si from  $\text{Ti}_3\text{SiC}_2$  and subsequent formation

of  $\text{TiC}_x$ .<sup>31,32</sup> Traces of  $\text{TiSi}_2$  were observed which might have formed due to the reaction between deintercalated Si and  $\text{Ti}_3\text{SiC}_2$ .

The density of the CMCs was measured to be above 99% of the theoretical value as calculated by considering the initial volume fraction of  $\text{Ti}_3\text{SiC}_2$  and  $\text{SiC}_w$ . The formation of TiC (4.93 g/cm<sup>3</sup>) and  $\text{TiSi}_2$  (4.02 g/cm<sup>3</sup>) by apparent decomposition does not affect the calculated density because of the countercompensation of new phases resulting in an aggregate with the same density of  $\text{Ti}_3\text{SiC}_2$ . The presence of TiC and  $\text{Al}_2\text{O}_3$  might affect the creep behavior of the CMCs, but the content of TiC and  $\text{Al}_2\text{O}_3$  is same in samples with different volumes of  $\text{SiC}_w$ , hence a comparison can be made. The change in the intensity ratio of the peaks at 39.5 and 40.8  $2\theta$  positions is due to the evolution of a crystallographic texture during sintering of  $\text{Ti}_3\text{SiC}_2$ . As pointed out earlier, the present study is about the influence of  $\text{SiC}_w$  on the creep resistance of  $\text{Ti}_3\text{SiC}_2$ -based CMCs and hence we will ignore here the effect of texture on the creep of  $\text{Ti}_3\text{SiC}_2$  and the creep is measured only in the direction perpendicular to the basal plane orientation.

Figure 2A-C show the microstructure of SPSed TSC, TSC-10 $\text{SiC}_w$ , and TSC-20 $\text{SiC}_w$  after polishing a face perpendicular to the direction of external pressure applied during sintering. The dispersion of  $\text{SiC}_w$  is homogeneous in TSC-10 $\text{SiC}_w$ , whereas an increase in  $\text{SiC}_w$  resulted in agglomeration in TSC-20 $\text{SiC}_w$ . However, the  $\text{Ti}_3\text{SiC}_2$  matrix phase was infiltrated into the  $\text{SiC}_w$  agglomerates. There were no pores observed in any of the composition and this was beneficial for the evaluation of creep in further investigation. Alumina inclusions can be seen as the dark grains and may result in the increase in the hardness and decrease in the fracture toughness and flexural strength of  $\text{Ti}_3\text{SiC}_2$ .<sup>33</sup> The effect of alumina

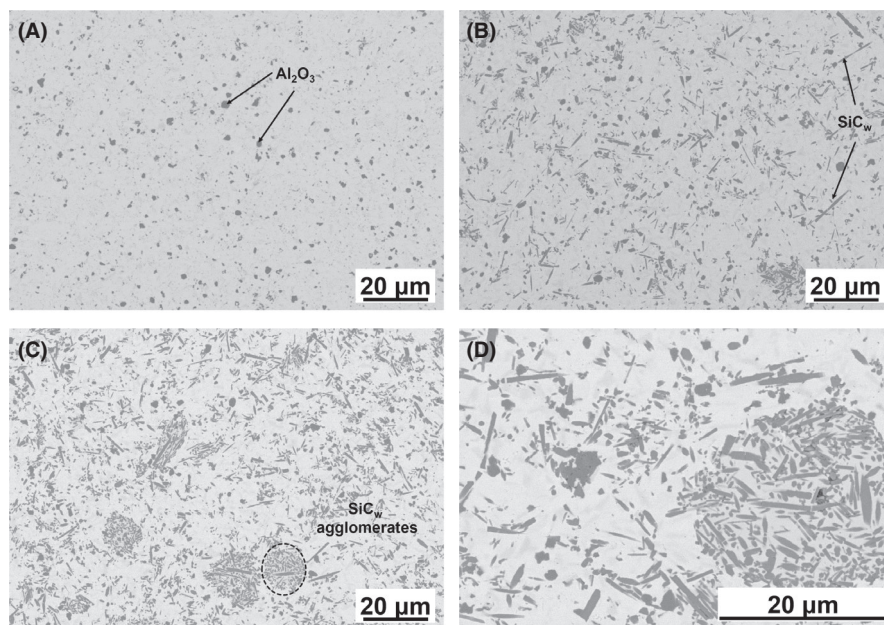


**FIGURE 2** Microstructure of SPS sintered  $\text{Ti}_3\text{SiC}_2$  (A), with 10 vol%  $\text{SiC}_w$  (B), and 20 vol%  $\text{SiC}_w$  (C), and higher magnification of the composite with 20 vol% of  $\text{SiC}_w$  (D)

on the creep response is unknown at the moment, however, it is expected to improve the creep resistance.

Figure 3 reveals the grain shape and  $\text{SiC}_w$  orientation in the direction perpendicular to the direction of uniaxial pressure during sintering. The high vacuum during sintering might be responsible for the evaporation of Si from the crystal structure of  $\text{Ti}_3\text{SiC}_2$ -forming TiC. Figure 3C,D depicts the phase map of TSC and TSC-20 $\text{SiC}_w$  corresponding to Figure 3A,B. The presence of TiC on the grain boundaries supports the assumption of Si depletion from the grain boundaries in vacuum at high temperature. Small amount of  $\text{TiSi}_2$  resulting from the decomposition of  $\text{Ti}_3\text{SiC}_2$  is visible in the grain boundaries of TSC, whereas it is not visible in TSC-20 $\text{SiC}_w$ . This can be related to the reaction of  $\text{TiSi}_2$  with  $\text{SiC}_w$  to form  $\text{Ti}_3\text{SiC}_2$  as  $\text{SiC}$  is also used as a precursor for the synthesis of  $\text{Ti}_3\text{SiC}_2$ .<sup>2</sup> The presence of TiC may have an effect on the creep of the material, but it is believed to behave similar to that of pure  $\text{Ti}_3\text{SiC}_2$  because of the continuous percolation of  $\text{Ti}_3\text{SiC}_2$ . Similar results were reported by Spencer et al with 16 vol% of TiC in  $\text{Ti}_3\text{SiC}_2$  as compared to 8.8 wt% TiC in the present case.<sup>34</sup>

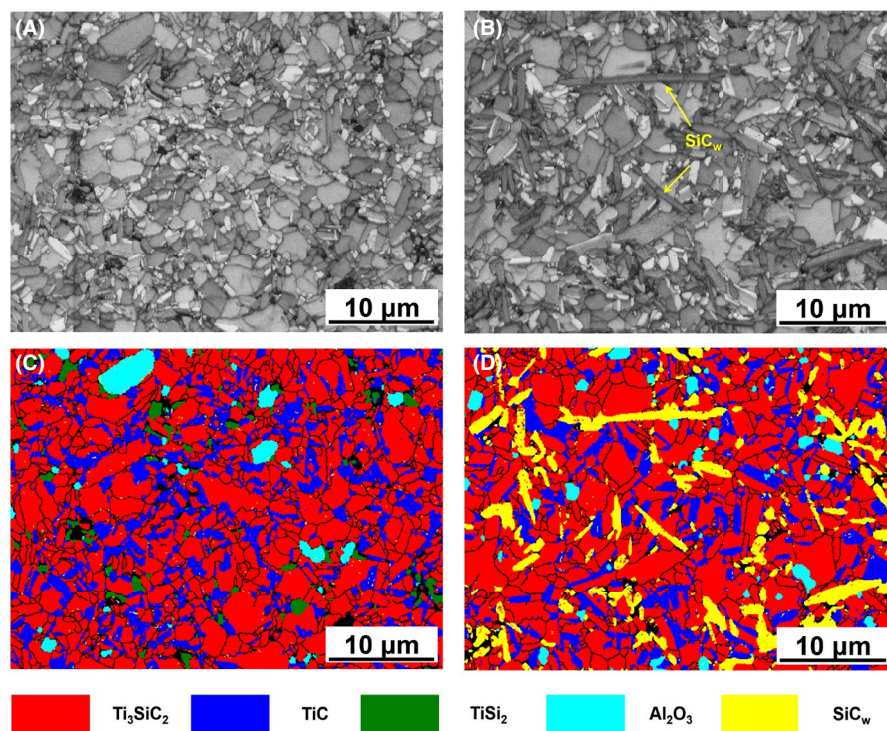
The orientation of  $\text{SiC}_w$  may be beneficial for the creep resistance because the deformation due to compressive stress is in lateral direction which is same as that of whisker alignment. The microstructures of the CMCs on the perpendicular face are equiaxed with an average grain size of  $1.2 \pm 0.6 \mu\text{m}$  of the  $\text{Ti}_3\text{SiC}_2$  phase, irrespective of the  $\text{SiC}_w$  content. The grain size is much smaller than the initial particle size ( $6 \mu\text{m}$ ) of the  $\text{Ti}_3\text{SiC}_2$  powder, this is probably due to the measurement of agglomerate size instead of the primary particle size in the case of the powder.

Examples of creep curves of  $\text{SiC}_w$ -reinforced  $\text{Ti}_3\text{SiC}_2$ -based CMCs for temperatures of 1200 and 1300°C under 20 MPa are shown in Figure 4A,B, respectively. The creep curves<sup>4</sup> can be separated into three stages being representative of (a) primary creep regime with a rapidly decreasing creep rate also known as transient creep stage; (b) secondary creep regime (steady state creep) with a constant creep rate, it is this regime which is of interest and is considered for evaluation of the creep properties of the CMCs fabricated in this work. The tests were aborted before reaching the (c) tertiary creep regime.

Since the creep testing was performed in air, the surface was oxidized because of very long dwell time at high temperature ( $>1000^\circ\text{C}$ ). However, the reduction in cross-section area is not significant and is same for all the CMC with different  $\text{SiC}_w$  content. Hence, we have neglected the effect of oxide scale ( $\sim 200 \mu\text{m}$ ) on the evaluation of creep data.<sup>4,24</sup> To assess the effect of oxide scale on creep, some creep tests were conducted in the cooling cycle for the sake of comparison. For example, the creep rate of TSC-10 $\text{SiC}_w$  at 1200°C and 40 MPa during heating from room temperature to 1300°C was compared with the same creep conditions but during cooling from 1300°C to room temperature. At 1300°C the oxidation of the sample is more imminent and might influence the creep but the creep rates during heating and cooling were approximately the same. It is worth noting that the formation of oxide scales on the surface plays an important role in the healing of the surface defects and scratches which in turn may result in a better creep resistance.<sup>35-37</sup>

The addition of  $\text{SiC}_w$  has a profound effect on the creep resistance of  $\text{Ti}_3\text{SiC}_2$ . TSC-20 $\text{SiC}_w$  is much more resistant to deformation as compared to monolithic  $\text{Ti}_3\text{SiC}_2$

**FIGURE 3** Microstructure of spark plasma sintering-sintered  $\text{Ti}_3\text{SiC}_2$  (A) and 20 vol%  $\text{SiC}_w$ -reinforced  $\text{Ti}_3\text{SiC}_2$  (B) obtained by band contrast of kikuchi pattern during electron backscattered diffraction data acquisition. Phase map of monolithic  $\text{Ti}_3\text{SiC}_2$  (C) and 20 vol%  $\text{SiC}_w$ -reinforced  $\text{Ti}_3\text{SiC}_2$  (D) corresponding to micrographs (A) and (B), respectively [Correction added on July 07, 2020, after first online publication: Figure 3 has been updated] [Color figure can be viewed at [wileyonlinelibrary.com](http://wileyonlinelibrary.com)]





or TSC-10SiC<sub>w</sub>. The inset shows magnified creep curves during the primary stage. TSC-10SiC<sub>w</sub> and TSC-20SiC<sub>w</sub> have similar deformation at 1200 and 20 MPa, whereas TSC and TSC-10SiC<sub>w</sub> have their creep curves close to each other at 1300°C and 20 MPa. The deformation of TSC-10SiC<sub>w</sub> is not intermediate to that of TSC and TSC-20SiC<sub>w</sub> and, hence, the addition of SiC<sub>w</sub> leads to a nonlinear effect on the increase in creep resistance, being an indication of different activation energies and/or stress exponents as will be discussed further.

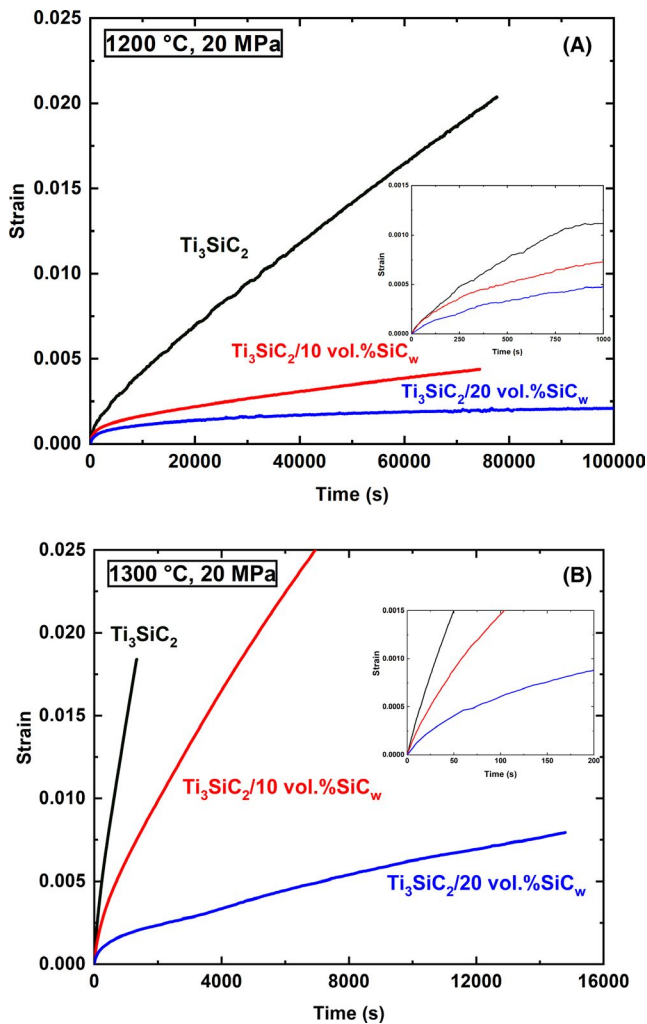


**FIGURE 4** Compressive creep curves of Ti<sub>3</sub>SiC<sub>2</sub>-based ceramic matrix composites at 1200°C, 20 MPa (A) and 1300°C, 20 MPa (B) [Color figure can be viewed at [wileyonlinelibrary.com](http://wileyonlinelibrary.com)]

**TABLE 1** Summary of activation energies for creep of TSC and SiC<sub>w</sub> reinforced Ti<sub>3</sub>SiC<sub>2</sub> composites in compression

Sample ID	Q (kJ/mol)	Stress exponents		
		1100°C	1200°C	1300°C
TSC	696 ± 16	3.0 ± 0.1		
TSC-10SiC <sub>w</sub>	652 ± 10	3.4 ± 0.03	4.1 ± 0.01	4.6 ± 0.3
TSC-20SiC <sub>w</sub>	665 ± 32			

The creep curves of pure and SiC<sub>w</sub>-reinforced Ti<sub>3</sub>SiC<sub>2</sub> in the temperature range 1100–1300°C at 40 and 80 MPa are shown in the Figure S1. At higher temperature (1300°C, 40 MPa, Figure S1C), the primary creep regime is indistinguishable for TSC and at higher loads with high temperature (1300°C, 80 MPa, Figure S1F), the primary creep is concealed even for TSC-20SiC<sub>w</sub>.

The steady-state creep rate  $\dot{\epsilon}$  was obtained by measuring the slope of the fitted straight line in the steady-state regime of the creep curves with time as the x-axis and creep strain as the y-axis. The activation energy and the stress exponent values were calculated by using the following relation<sup>38</sup>

$$\dot{\epsilon} = \dot{\epsilon}_0 A \left( \frac{\sigma}{\sigma_0} \right)^n \exp \left( -\frac{Q}{RT} \right), \quad (1)$$

where  $A$ ,  $n$ , and  $Q$  are dimensionless constant, stress exponent, and activation energy, respectively.  $\dot{\epsilon}_0$  and  $\sigma_0$  are 1 s<sup>-1</sup> and 1 MPa used for defining the dimensions of strain rate and stress. The slope of straight lines plotted by fitting the data of minimum creep rate with respect to inverse of absolute temperature and  $\ln$  of the applied stress gives the activation energy and stress exponent, respectively. Equation (1) is simplified into straight line equation ( $y = mx + c$ ) by applying the natural logarithm on both sides of the equation, where  $m$  accounts for the slope of the fitted line.

Figure 4A presents Arrhenius plots of the steady-state creep rate vs the reciprocal absolute temperature for different applied stresses. Regression analysis of the data was carried out via a global fit of all data using the software Origin to obtain the activation energies for the considered temperature range 1100–1300°C.

A simplified bootstrap type analysis was done by deleting individual data points and performing a fit of the rest of the data points to identify if specific data points cause an increase in scatter of the activation energy. It was found that the data points for TSC-10SiC<sub>w</sub> at 1100°C and 20 MPa corresponded to a creep of 1 μm/d and is probably still in primary creep regime, hence, it was excluded for the calculation of activation energy, the same was done for TSC-20SiC<sub>w</sub> at 1100°C and 40 MPa.

The calculated activation energies for the CMCs are summarized in Table 1. Upon the addition of SiC<sub>w</sub> there is reduction in activation energy from 696 ± 16 kJ/mol for monolithic Ti<sub>3</sub>SiC<sub>2</sub> to 665 ± 31 kJ/mol for TSC-20SiC<sub>w</sub> with

a similar value for the material with 10 vol% whisker, so the addition of  $\text{SiC}_w$  results in  $\sim 10\%$  lower activation energy, which is, however, within the limits of experimental uncertainty. A lower activation energy simply means a change in creep rate controlling process and has no strict implication toward the resistance to creep of a material, however, more indications with respect to the active creep mechanism is provided by the stress exponent values. Hence, the overall activation energies of three compositions are similar and the rate controlling factor can be assumed to be almost the same as well.

Ln-ln plots of steady-state creep as a function of applied stress for different temperatures are given in Figure 5. The stress exponents ( $n$ ) were calculated by a linear regression analysis of the data. A global fit of the creep rates of TSC and TSC-10 $\text{SiC}_w$  was performed, whereas, for TSC-20 $\text{SiC}_w$ , individual fits were performed since the global fit with TSC-20 $\text{SiC}_w$  resulted in large scatter.

The stress exponents of every composition are compared in Table 1 for the different temperatures. The increasing values of stress exponents of TSC-20 $\text{SiC}_w$  clearly indicate a transition of the creep mechanism for TSC-20 $\text{SiC}_w$  at different temperatures.

With the addition of 10 vol% of  $\text{SiC}_w$  addition there is a reduction in the creep rate by two orders of magnitude. There is no temperature dependency of the stress exponent for TSC and TSC-10 $\text{SiC}_w$ , hence, the creep mechanism is expected to be same over the whole temperature range. On the other hand, TSC-20 $\text{SiC}_w$  has a strong temperature dependency and the stress exponent increases from 3.4 at 1100°C to 4.6 at 1300°C.

Fractured surfaces of creep-tested samples are shown in the Figure S2. The TSC samples show delamination, whereas CMCs with  $\text{SiC}_w$  show rather kinking and bending of grains (Figure S2A-C).

## 4 | DISCUSSION

### 4.1 | Microstructure development of MAX phase-based CMCs

Pressure-assisted sintering of hexagonal materials normally yields an anisotropic microstructure. Whether the  $c$ -axis is aligned perpendicular<sup>39</sup> or parallel<sup>40</sup> to the pressing direction is material dependent. It was reported by Tang et al that the basal plane of  $\text{Ti}_3\text{SiC}_2$  grains prefers a nonparallel alignment with the pressing surface, which implies that the  $c$ -axis is preferably aligned perpendicular to the pressing direction,<sup>41</sup> however, the opposite is observed in the present case. Since the starting powder had platelet morphology, a plate-like microstructure was to be expected. TSC-10 $\text{SiC}_w$  was selected for microstructural investigation assuming TSC-20 $\text{SiC}_w$  will

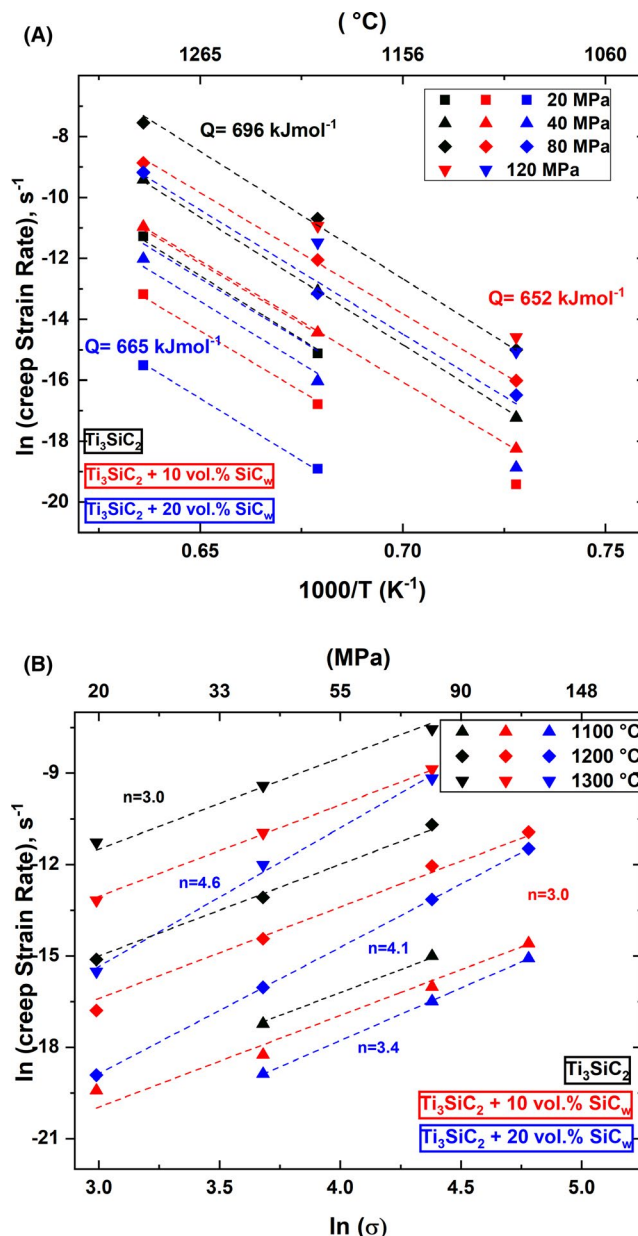


**FIGURE 5** Ln plot of min. strain rate as (A) a function of temperature and as (B) a function of applied compressive stress for  $\text{Ti}_3\text{SiC}_2$  MAX phase-based ceramic matrix composites with varying content of  $\text{SiC}_w$  for compressive creep measured at stress levels of 20–120 MPa [Color figure can be viewed at [wileyonlinelibrary.com](http://wileyonlinelibrary.com)]

have similar microstructure with a higher content of  $\text{SiC}_w$  only. There was no difference in average grain size expected because the sintering was performed at a low temperature (1250°C).

Figure 6A shows the microstructure of TSC-10 $\text{SiC}_w$  perpendicular to the pressing direction. Clearly, the sintered TSC-10 $\text{SiC}_w$  has a texture due to the applied uniaxial external pressure and the rearrangements of the platelets under high temperature and pressure to attain a high density. The  $c$ -axis is parallel to the pressing direction (Figure 6B). As expected, the  $\text{SiC}_w$  is also oriented perpendicular to the



**FIGURE 6** Microstructure and orientation map of as-sintered (A, B) and postcreep (C, D)  $\text{Ti}_3\text{SiC}_2$ -10 vol%  $\text{SiC}_w$  composites. The microstructure investigation is done on a perpendicular face with respect to the direction of the applied external pressure for sintering. Note, the  $\text{SiC}_w$  is cutting through  $\text{Ti}_3\text{SiC}_2$  grain during creep at  $1300^\circ\text{C}$ , 80 MPa (yellow arrows in Figure 6C) [Color figure can be viewed at [wileyonlinelibrary.com](http://wileyonlinelibrary.com)]

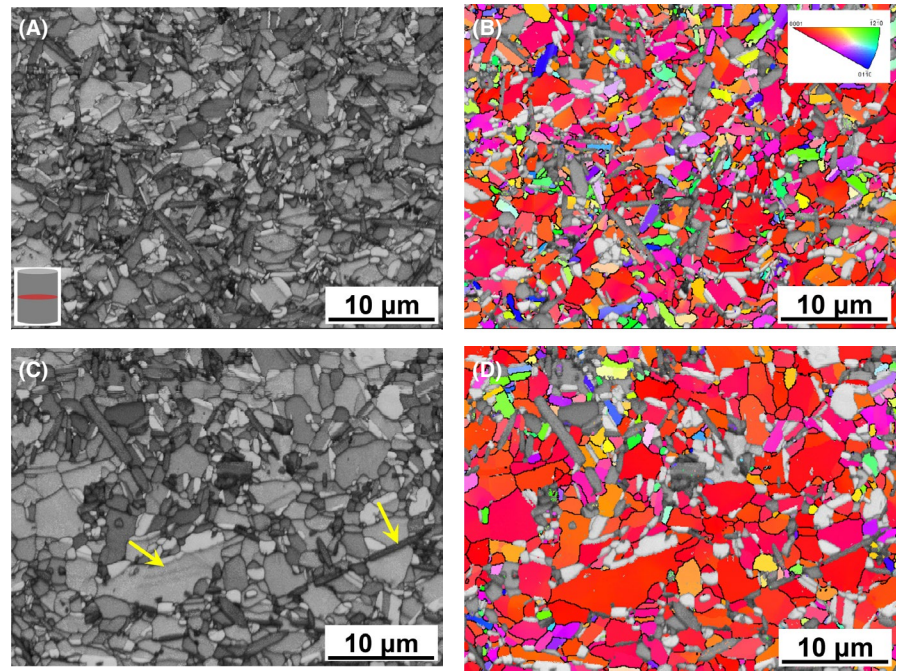
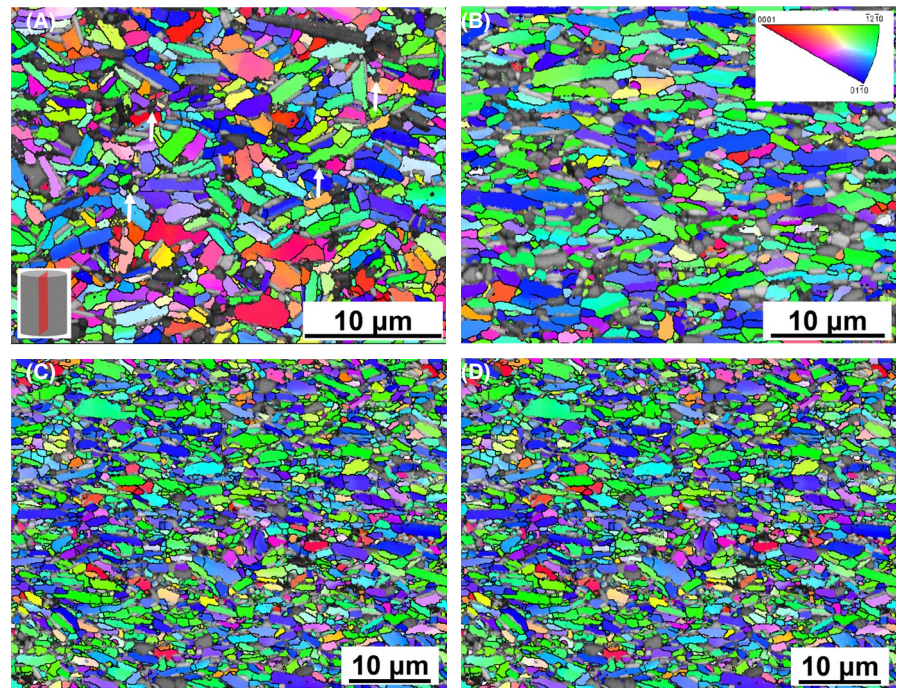


**FIGURE 7** Orientation map of as-sintered (A, C) and postcreep (B, D) ( $1300^\circ\text{C}$ , 80 MPa)  $\text{Ti}_3\text{SiC}_2$ -10 $\text{SiC}_w$  (A, B) and  $\text{Ti}_3\text{SiC}_2$  (C, D). The microstructure investigation is done on a parallel face with respect to the direction of the applied compressive stress for creep. Please note that A–D are images with different magnification and it is not to be confused with different grain size. Note the white arrows in Figure 7A showing the tips of  $\text{SiC}_w$  [Color figure can be viewed at [wileyonlinelibrary.com](http://wileyonlinelibrary.com)]



pressing direction and the orientation of the whiskers can be considered as random within the perpendicular plane.<sup>42</sup> In Figure 7A, only the tips of  $\text{SiC}_w$  are visible, hence are not identifiable as entities with high aspect ratio (white arrows). The  $\text{Ti}_3\text{SiC}_2$  grains on the face perpendicular to pressing direction are equiaxed, whereas on the face parallel to pressing direction the grains were elongated with an aspect ratio  $\sim 10$ .

Since the microstructure is anisotropic, the grain size and morphology of parallel and perpendicular face with respect to pressing direction are also different. The equivalent grain

size is calculated by Relation (2).<sup>42</sup> The effective grain size can be derived from:

$$\frac{4}{3}\pi \left(\frac{d_{\perp}}{2}\right)^2 \left(\frac{d_{\parallel}}{2}\right) = \frac{4}{3}\pi \left(\frac{d_{\text{eff}}}{2}\right)^3 \Rightarrow d_{\text{eff}} = \sqrt[3]{d_{\perp}^2 d_{\parallel}}, \quad (2)$$

where  $d_{\perp}$  and  $d_{\parallel}$  are the average grain size of perpendicular and parallel face, respectively. Although the grain morphology was different comparing the parallel and perpendicular face, the average grain size calculated by the projected area diameter was



similar for both faces and the effective grain size was always calculated to be  $1.2 \pm 0.6 \mu\text{m}$ .

Unlike expected, the addition of  $\text{SiC}_w$  did not result in any grain size refinement due to the absence of grain growth of the starting  $\text{Ti}_3\text{SiC}_2$  powder owing to the low sintering temperature. For comparison, the orientation of monolithic  $\text{Ti}_3\text{SiC}_2$  in the parallel direction of applied stress is shown in Figure 7C. It can be noted that the anisotropy of monolithic  $\text{Ti}_3\text{SiC}_2$  after sintering is higher than TSC-10 $\text{SiC}_w$ . The  $\text{Ti}_3\text{SiC}_2$  grains are aligned in the direction perpendicular to the applied uniaxial stress for sintering. The degree of alignment of  $\text{Ti}_3\text{SiC}_2$  platelets is higher because of absence of any  $\text{SiC}_w$  which might have restricted grain rearrangement during sintering.

## 4.2 | Creep deformation mechanism

The creep deformation mechanisms of composite materials are difficult to decipher by only measuring activation energies and stress exponents. Activation energies of all compositions agree within the limits of experimental uncertainty. The stress exponent of TSC and TSC-10 $\text{SiC}_w$  is around 3 and is constant over the whole temperature range (1100–1300°C), whereas for TSC-20 $\text{SiC}_w$  the stress exponents increase with increasing temperature.

Stress exponents of 3–5 indicate dislocation climb as the rate controlling mechanism. In addition, the deformation process also involves dislocation glide due to shear stress acting normal to the applied uniaxial stress during creep test.<sup>43</sup> The rate control mechanism of both monolithic and reinforced  $\text{Ti}_3\text{SiC}_2$  MAX phases is similar due to similar activation energies, but the exact rate controlling mechanism of the CMCs is not clear.

In case of TSC-10 $\text{SiC}_w$ , GBS is evident by the change in the grain direction and alignment of the basal plane normal to the applied stress during creep (compare Figure 7A,B). Some basal planes which were visible in Figure 7A (TSC-10 $\text{SiC}_w$  precreep) disappeared after creep in Figure 7B (TSC-10 $\text{SiC}_w$  postcreep). There appears not to be any GBS in case of TSC, which can be concluded from the grain shape before and after creep, which is further supported by grain orientation data by EBSD (Figure 7C,D).

The evidence of the presence of GBS in TSC-10 $\text{SiC}_w$  is also provided by the evolution of low-angle grain boundary (LAGB) in TSC-10 $\text{SiC}_w$  after creep (Figure S3).<sup>44</sup> This appears to be a clear case of grain rotation during high-temperature deformation.<sup>45</sup> In the case of TSC, the misorientation angle distribution remains the same after creep.

It is now well known that dislocations exist in basal planes of MAX phases and these dislocations also form a LAGB normal to the basal plane and this is observed in the current work as well.<sup>21</sup> The  $\text{SiC}_w$  may limit GBS

by interlocking the  $\text{Ti}_3\text{SiC}_2$  grains.<sup>46</sup> With the increase in  $\text{SiC}_w$  content, the creep resistance simply increases because of reduction in the amount of plastic phase in the composite.

The basal plane is aligned perpendicular to the pressing direction and so is the  $\langle 0001 \rangle$  direction. Although fine-grained  $\text{Ti}_3\text{SiC}_2$  is not susceptible to deformation as their coarse-grain counterparts, during creep kinking also might have played a role to absorb the mechanical stress during creep. The shear of (0001) plane is difficult because it involves the breaking of Ti–C bonds, whereas the Ti–Si bond is more susceptible to break. Hence, a preferential dislocation glide can be the mechanism favored along the basal plane.<sup>47</sup> As the material has a high fraction of grains with their basal plane aligned perpendicular to the compression direction, there is also a higher possibility of basal plane shear.

For temperatures  $< 1300^\circ\text{C}$  and low stresses ( $< 40 \text{ MPa}$ ), the presence of  $\text{SiC}_w$  reduces the creep, whereas the increase in the content of  $\text{SiC}_w$  (from 10 to 20 vol%) has only a subtle decrease in the creep rates (Figure 4), suggesting the extra 10 vol%  $\text{SiC}_w$  does not efficiently inhibit GBS rather, this might imply dislocation creep as one of the mechanism in case of  $\text{SiC}_w$ -reinforced  $\text{Ti}_3\text{SiC}_2$ . The presence of rigid  $\text{SiC}_w$  may have restricted GBS of  $\text{Ti}_3\text{SiC}_2$  partially or completely and hence resulted in a smaller deformation and creep rate.<sup>42</sup> Since the aspect ratio of the  $\text{SiC}_w$  is  $\sim 10$ , the critical percolation limit volume fraction ( $\phi_{\text{pcp}}$ ) is around 7% as calculated by the following relation:<sup>48</sup>

$$\phi_{\text{pcp}} = \frac{0.7}{\text{aspect ratio}}, \quad (3)$$

where  $\phi_{\text{pcp}}$  is the limit above which the whiskers can form an interconnected network. Since the materials are sintered under uniaxial pressure, there is a lack of three-dimensional connectivity (percolation) of  $\text{SiC}_w$ , rather there are two-dimensional arrays of  $\text{SiC}_w$  perpendicular to the uniaxial stress during sintering.  $\phi_{\text{pcp}}$  for such materials can be larger by a factor of 2 because Expression (2) holds true for only randomly oriented whiskers.<sup>49</sup> Considering a  $\phi_{\text{pcp}}$  of 14%, the content of  $\text{SiC}_w$  used in the present study is both below (TSC-10 $\text{SiC}_w$ ) and above (TSC-20 $\text{SiC}_w$ ) percolation limit. The fact that the stress exponent of TSC-20 $\text{SiC}_w$  becomes larger at high temperature indicates that the property for this material under this condition is not a general material representative rather representative for material under specific conditions only.

The increasing stress exponents of TSC-20 $\text{SiC}_w$  provide the evidence of a change in creep mechanism over the temperature range 1100–1300°C, whereas for TSC and TSC-10 $\text{SiC}_w$  the creep mechanism is same across the entire temperature range.

At 1200°C, 20 MPa, the addition of SiC<sub>w</sub> may have restricted GBS and hence the lower deformation and creep rates of TSC-10SiC<sub>w</sub> and TSC-20SiC<sub>w</sub>. Although fine-grained Ti<sub>3</sub>SiC<sub>2</sub> has a brittle to plastic (BTP) transition at ~1200°C, the creep resistance is enhanced by the addition of SiC<sub>w</sub>.<sup>50</sup> Since the addition of SiC<sub>w</sub> has an increase in the creep resistance of Ti<sub>3</sub>SiC<sub>2</sub>, grain boundary diffusion may have been hindered.

At a temperature of >1200°C, both lattice and grain boundary diffusion may have become significant as indicated by the BTP transition of Ti<sub>3</sub>SiC<sub>2</sub> and hence pile-up of dislocations can be reduced efficiently and so the addition of SiC<sub>w</sub> did not reduce the creep rates considerably at 1300°C. At temperature above 1200°C, where the Ti<sub>3</sub>SiC<sub>2</sub> has a BTP transition, the creep of CMCs (specifically TSC-20SiC<sub>w</sub>) can be viewed as a sequential viscoplastic and viscoelastic deformation. The viscoplastic creep refers to the approach of SiC<sub>w</sub> randomly oriented perpendicular to the creep direction. The matrix phase (Ti<sub>3</sub>SiC<sub>2</sub>) is squeezed out from between the in-plane SiC<sub>w</sub> network. The hard SiC<sub>w</sub> acts as lines of stress concentration which cuts through the soft Ti<sub>3</sub>SiC<sub>2</sub> grains.

The large arrows in Figure 6C show a grain with straight-edge grain boundary because of SiC<sub>w</sub> sinking into it and a cut Ti<sub>3</sub>SiC<sub>2</sub> grain with SiC<sub>w</sub> in the grain boundary. The distance between the randomly SiC<sub>w</sub> is stochastic and the lack of three-dimensional SiC<sub>w</sub> network is due to the perpendicular alignment of SiC<sub>w</sub> to the stress during sintering. For interconnectivity there should be a random angular distribution of SiC<sub>w</sub>, whereas it is not in the present case. The viscoplastic deformation ceases once the SiC<sub>w</sub> have point contacts within the perpendicularly oriented planes.

The elastic bending of SiC<sub>w</sub> with the deformation of Ti<sub>3</sub>SiC<sub>2</sub> in the immediate vicinity of the SiC<sub>w</sub> to accommodate the elastic deformation of SiC<sub>w</sub> is referred to as viscoelastic creep. The viscoplastic deformation is only if  $\phi \leq \phi_{pcp}$ , hence this is valid for TSC-10SiC<sub>w</sub>, whereas in the case of TSC-20SiC<sub>w</sub>, the SiC<sub>w</sub> network is responsible for decreased creep rate. The probable absence of any viscoplastic creep above 1200°C results in an increase in creep resistance of TSC-20SiC<sub>w</sub>. Since TSC-20SiC<sub>w</sub> has a SiC<sub>w</sub> content higher than  $\phi_{pcp}$ , the SiC<sub>w</sub> network inhibits GBS and the creep is governed by only diffusion, hence, it has lower creep rates as compared to TSC and TSC-10SiC<sub>w</sub>. However, beyond a certain stress TSC-20SiC<sub>w</sub> behaves different and the creep rates are not reduced to the same degree as at low stresses. This might be due to the interaction of agglomerates of SiC<sub>w</sub> present in the material.

### 4.3 | Transmission electron microscopy

The TEM micrographs of the crept specimen demonstrate various defects indicating the creep mechanism which it

underwent. The defects, dislocations, as well as grain structures visible in the microstructures have been elucidated to explain the formation of the dislocation structures and their mechanism. The most common defects visible in crept MAX phases are edge dislocations and stacking faults. The layered inherent character of MAX phases makes it prone to stacking faults during processing as well as deformation.<sup>51</sup> Stacking faults are diffusion-driven phenomenon which are evident in the vicinity of grain boundaries ending with partials.<sup>52</sup> Triangular cavitation can be observed, which is an implication of GBS. Polygonal cavitation is also visible on triple junctions of the specimen in Figure 8A. Size of cavities ranges from 50 to 60 nm; basal dislocation arrays are seen to be surrounding the cavitation. Dislocation pile up at the whiskers boundary is visible here; cavitation (triangular ones) was also observed by Barsoum et al in tensile crept specimen.<sup>24,44</sup> The faint grey contrast throughout the specimen is due to bending, curling, and kinking of the layers in the crept sample. Due to angular field of view, we can see the kinks and bends as small curly entities. Stacking faults (Figure 8B) pertaining to basal plane are very often visible in MAX phase. Basal dislocation glide gives rise to formation of grain boundary steps. GBS is a failure mode which is evident from Figure 8C during creep, the layered nature of Ti<sub>3</sub>SiC<sub>2</sub> promotes sliding action of layers which also gives rise to GBS of the material. A curved grain with a kink band in the centre is shown in Figure 8C suggesting the presence of kinking during creep, although not in abundance. The basal planes generally form a curved surface to accommodate the grain boundary step formation. Grain boundary steps can be seen in Figure 8D which is a result of grain boundary glide planes during creep of the specimen which is an identified phenomenon in the past.<sup>44</sup> Hexagonal networks can be seen in Figure 8E along with complex dislocation network. Dislocation-dislocation interaction generally leads to dislocation reactions forming planar hexagonal networks which can be seen in Figure 8E. Figure 8F reveals whiskers embedded in the matrix surrounded by dislocation loop. Figure 8G demonstrates defects which are non-planar in nature. These defects are unusual to MAX phase and are a result of complex dislocation interactions and superimpositions. The inset shows selected area diffraction (SAD) pattern pertaining to basal plane of the MAX phase showing sixfold symmetry and some amount of streaking due to layer morphology of Ti<sub>3</sub>SiC<sub>2</sub>.

The SiC<sub>w</sub> (bright white areas) can be seen impeding the dislocation movement, the Figure 9A shows the pile up of dislocations near the SiC<sub>w</sub>. Figure 9B,C shows a dislocation network in the vicinity of the SiC<sub>w</sub> entities. The dislocation pile up around the whiskers proves that they impede the dislocation movement in the Ti<sub>3</sub>SiC<sub>2</sub> matrix. Edge dislocations are visible in ample number in the matrix, interacting with each



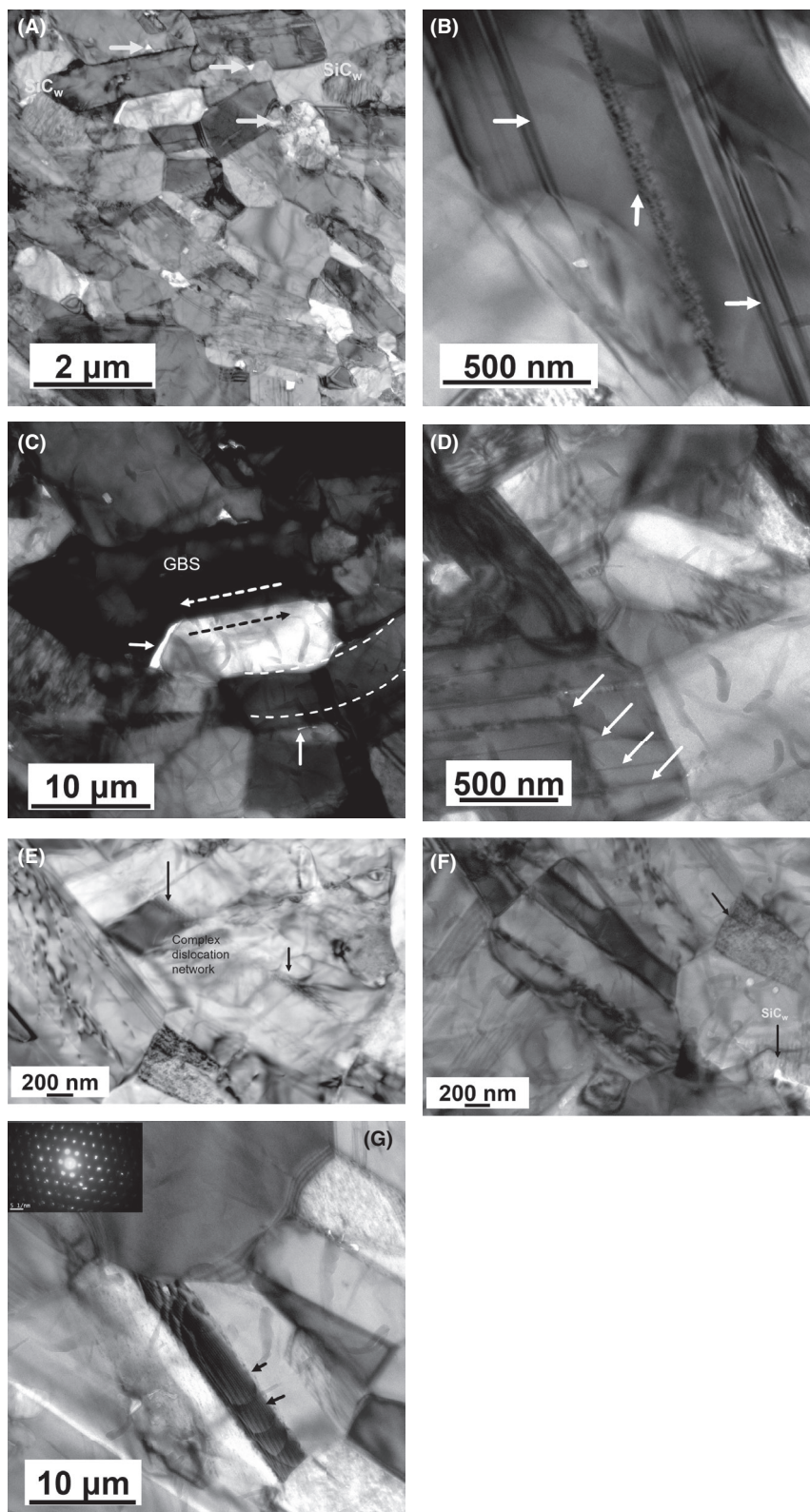


**FIGURE 8** Bright-field transmission electron microscopy images of postcreep (1300°C, 80 MPa)  $\text{Ti}_3\text{SiC}_2$ -10 $\text{SiC}_w$  showing cavitations (A), stacking faults (B), grain boundary sliding (C, D), complex dislocation network, and defects formed during creep (E-G). White arrows in Figure 8A, 8B, 8C and 8D denotes cavitation due to creep, stacking faults, cavitation due to GBS and grain boundary steps due to creep respectively. The curved grain in Figure 8C is a result of kinking during creep and is denoted by curved white dashed lines. The black arrows in Figure 8G denotes complex dislocation interactions

**FIGURE 9** Bright-field scanning transmission electron microscopy images of postcreep (1300°C, 80 MPa)  $\text{Ti}_3\text{SiC}_2$ -20 $\text{SiC}_w$  showing the distribution of  $\text{SiC}_w$  (A), dislocation entanglement (B), and dislocation pile-up at the  $\text{Ti}_3\text{SiC}_2$ - $\text{SiC}_w$  interface (C) and (D) [Color figure can be viewed at [wileyonlinelibrary.com](http://wileyonlinelibrary.com)]

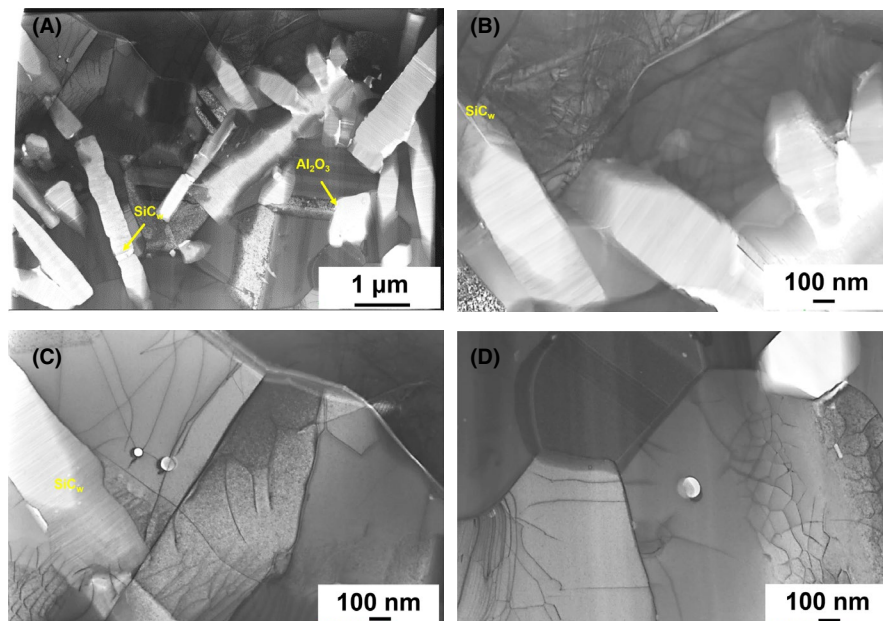


**TABLE 2** Summary of creep activation energy and stress exponents for  $\text{Ti}_3\text{SiC}_2$  in compression with comparison to the previously investigated results

Material	Q (kJ/mol)	n	Proposed mechanism	Reference
TSC (in compression)	$537 \pm 31$	1.9	Dislocation	[4]
TSC (in tension)	$445 \pm 10$	1.5	Plastic deformation	[20]
TSC	$696 \pm 16$	3	Dislocation	This work
TSC-10 $\text{SiC}_w$	$652 \pm 10$	3	Dislocation, GBS, and viscoplastic	This work
TSC-20 $\text{SiC}_w$	$665 \pm 32$	3.4-4.6	Dislocation, viscoplastic, and viscoelastic	This work

Abbreviations: GBS, grain boundary sliding; TSC,  $\text{Ti}_3\text{SiC}_2$ .

other and are operating in loops around the whiskers as well as the  $\text{Ti}_3\text{SiC}_2$  phase (Figure 9D). The network of dislocations can be attributed to common dislocation reactions operative in hcp materials, ie,  $1/3[11-20] + 1/3[-2110] = 1/3[-12-10]$ . Deformation by creep induces these dislocation networks which indicates grain rotation. Figure 9D shows dislocation cells formation which is a sign of recovery during creep. There were no features identified in the case of TSC-20 $\text{SiC}_w$  implying GBS as in the case of TSC-10 $\text{SiC}_w$ . Transmission kikuchi diffraction of the lamella in Figure S4 reveals that the grains with nonbasal orientation also have dislocations present in them.

As compared to the data reported in the literature (Table 2), the activation energy and stress exponents of  $\text{Ti}_3\text{SiC}_2$  are higher, this might be attributed to the high anisotropy and texture present in the currently investigated monolithic  $\text{Ti}_3\text{SiC}_2$ . Monolithic  $\text{Ti}_3\text{SiC}_2$  is believed to undergo pure dislocation creep, whereas TSC-10 $\text{SiC}_w$  undergoes a combination of dislocation creep, GBS, and viscoplastic creep. This has been shown and correlated by the postcreep EBSD and

TEM analysis. TSC-20 $\text{SiC}_w$  can be assumed to have undergone a combination of dislocation creep, viscoplastic creep, and viscoelastic creep. Although the proposed mechanism for monolithic material and composites with partial evidences are different from each other, the rate controlling creep mechanism is believed to be mainly dislocation based and hence all the materials has similar activation energies. Moreover, the transition in the creep mechanism of TSC-20 $\text{SiC}_w$  is supported by the change in stress exponent over the temperature range.

## 5 | CONCLUSION

$\text{Ti}_3\text{SiC}_2$ -based CMCs were fabricated by reinforcing with  $\text{SiC}_w$  and sintering the same to full density by SPS. The grain size of the CMCs irrespective of  $\text{SiC}_w$  content was measured to be  $1.2 \pm 0.6 \mu\text{m}$ . The dispersion of  $\text{SiC}_w$  was uniform for TSC-10 $\text{SiC}_w$ , whereas for TSC-20 $\text{SiC}_w$  there were agglomerations of  $\text{SiC}_w$ . The compressive creep of the composites was carried out in air in the temperature




range 1100–1300°C and stress level from 20 to 120 MPa. The creep rates were a function of the  $\text{SiC}_w$  content and decreased with increasing  $\text{SiC}_w$ . The stress exponent of TSC and TSC-10 $\text{SiC}_w$  was constant over the range of temperatures but that of TSC-20 $\text{SiC}_w$  increased with increasing temperature from 3.4 at 1100°C to 4.6 at 1300°C. The creep mechanism of monolithic  $\text{Ti}_3\text{SiC}_2$  is believed to be dislocation creep, whereas for composites, a combination of dislocation creep and GBS is believed to be the deformation mechanism.  $\text{SiC}_w$  inhibited the GBS by anchoring grains together; a higher content of  $\text{SiC}_w$  in  $\text{Ti}_3\text{SiC}_2$  might be responsible for creating a network of particles resulting in higher creep resistance. A combination of viscoplastic and viscoelastic creep can be operating during the creep of TSC-20 $\text{SiC}_w$ .

## ACKNOWLEDGMENTS

This work was funded by Germany's Federal Ministry of Education and Research (Bundesministerium für Bildung und Forschung) under the MAXCOM project (03SF0534). The authors would like to thank Dr Egbert Wessel for EBSD investigations and Marcel Turiaux for assistance in creep measurements.

## ORCID

Apurv Dash  <https://orcid.org/0000-0002-4869-3104>

Jesus Gonzalez-Julian  <https://orcid.org/0000-0002-4217-8419>

## REFERENCES

- Barsoum MW. MAX phases: properties of machinable ternary carbides and nitrides. Weinheim, Germany: Wiley-VCH Verlag GmbH & Co. KGaA, 2013; p. 1–421. Available from <https://doi.org/10.1002/9783527654581>
- Barsoum MW, El-Raghy T. Synthesis and characterization of a remarkable ceramic:  $\text{Ti}_3\text{SiC}_2$ . *J Am Ceram Soc.* 1996;79(7):1953–6.
- Chen D, Shirato K, Barsoum MW, El-Raghy T, Ritchie RO. Cyclic fatigue-crack growth and fracture properties in  $\text{Ti}_3\text{SiC}_2$  ceramics at elevated temperatures. *J Am Ceram Soc.* 2001;84(12):2914–20.
- Zhen T, Barsoum MW, Kalidindi SR, Radovic M, Sun ZM, El-Raghy T. Compressive creep of fine and coarse-grained  $\text{Ti}_3\text{SiC}_2$  in air in the 1100–1300°C temperature range. *Acta Mater.* 2005;53(19):4963–73.
- Radovic M, Barsoum MW, El-Raghy T, Wiederhorn SM. Tensile creep of coarse-grained  $\text{Ti}_3\text{SiC}_2$  in the 1000–1200°C temperature range. *J Alloys Compd.* 2003;361(1–2):299–312.
- Zhen T, Barsoum MW, Kalidindi SR. Effects of temperature, strain rate and grain size on the compressive properties of  $\text{Ti}_3\text{SiC}_2$ . *Acta Mater.* 2005;53(15):4163–71.
- Radhakrishnan R, Williams J, Akinc M. Synthesis and high-temperature stability of  $\text{Ti}_3\text{SiC}_2$ . *J Alloys Compd.* 1999;285(1–2):85–8.
- Lenz F, Krenkel W. Fabrication of fiber composites with a MAX phase matrix by reactive melt infiltration. *IOP Conf Ser Mater Sci Eng.* 2011;18(20):202030.
- Mu Y, Zhou W, Hu Y, Qing Y, Luo F, Zhu D. Improvement of mechanical and dielectric properties of PIP-SiCf/SiC composites by using  $\text{Ti}_3\text{SiC}_2$  as inert filler. *Ceram Int.* 2015;41(3):4199–206.
- Yin X, He S, Zhang L, Fan S, Cheng L, Tian G, et al. Fabrication and characterization of a carbon fibre reinforced carbon-silicon carbide-titanium silicon carbide hybrid matrix composite. *Mater Sci Eng A.* 2010;527(3):835–41.
- Lagos MA, Pellegrini C, Agote I, Azurmendi N, Barcena J, Parco M, et al.  $\text{Ti}_3\text{SiC}_2$ -Cf composites by spark plasma sintering: processing, microstructure and thermo-mechanical properties. *J Eur Ceram Soc.* 2019;39(9):2824–30.
- Spencer CB, Córdoba JM, Obando NH, Radovic M, Odén M, Hultman L, et al. The reactivity of  $\text{Ti}_2\text{AlC}$  and  $\text{Ti}_3\text{SiC}_2$  with SiC fibers and powders up to temperatures of 1550°C. *J Am Ceram Soc.* 2011;94(6):1737–43.
- Gonzalez-Julian J, Llorente J, Bram M, Belmonte M, Novel GO.  $\text{Cr}_2\text{AlC}$  MAX-phase/SiC fiber composites: synthesis, processing and tribological response. *J Eur Ceram Soc.* 2017;37(2):467–75.
- Gonzalez-Julian J, Classen L, Bram M, Vaßen R, Near GO. Net shaping of monolithic and composite MAX phases by injection molding. *J Am Ceram Soc.* 2016;99(10):3210–13.
- Wan DT, Hu CF, Bao YW, Zhou YC. Effect of SiC particles on the friction and wear behavior of  $\text{Ti}_3\text{Si(Al)C}_2$ -based composites. *Wear.* 2007;262(7–8):826–32.
- Wan DT, Zhou YC, Bao YW, Yan CK. In situ reaction synthesis and characterization of  $\text{Ti}_3\text{Si(Al)C}_2$ /SiC composites. *Ceram Int.* 2006;32(8):883–90.
- Zhou YC, Wan DT, Bao YW, Wang JY, In WDT. Situ processing and high-temperature properties of  $\text{Ti}_3\text{Si(Al)C}_2$ /SiC composites. *Int J Appl Ceram Technol.* 2006;3(1):47–54.
- Li S, Song GM, Zhou Y. A dense and fine-grained SiC/ $\text{Ti}_3\text{Si(Al)C}_2$  composite and its high-temperature oxidation behavior. *J Eur Ceram Soc.* 2012;32(12):3435–44.
- Dash A, Malzbender J, Vaßen R, Guillon O, Gonzalez-Julian J. Short SiC fiber /  $\text{Ti}_3\text{SiC}_2$  MAX phase composites: Fabrication and creep evaluation. *Journal of the American Ceramic Society.* 2020. <http://dx.doi.org/10.1111/jace.17337>
- Li J-F, Pan W, Sato F, Watanabe R. Mechanical properties of polycrystalline  $\text{Ti}_3\text{SiC}_2$  at ambient and elevated temperatures. *Acta Mater.* 2001;49(6):937–45.
- Barsoum MW, Farber L, El-Raghy T. Dislocations, kink bands, and room-temperature plasticity of  $\text{Ti}_3\text{SiC}_2$ . *Metall Mater Trans A.* 1999;30(7):1727–38.
- Ren Z, Singh G. Nonoxide polymer-derived CMCs for “super” turbines. *Am Ceram Soc Bull.* 2019;98(3):34–9.
- Gupta S, Barsoum MW. On the tribology of the MAX phases and their composites during dry sliding: a review. *Wear.* 2011;271(9–10):1878–94.
- Radovic M, Barsoum M, El-Raghy T, Wiederhorn S. Tensile creep of fine grained (3–5  $\mu\text{m}$ )  $\text{Ti}_3\text{SiC}_2$  in the 1000–1200°C temperature range. *Acta Mater.* 2001;49(19):4103–12.
- Tallman DJ, Naguib M, Anasori B, Barsoum MW. Tensile creep of  $\text{Ti}_2\text{AlC}$  in air in the temperature range 1000–1150°C. *Scr Mater.* 2012;66(10):805–8.
- Araki W, Gonzalez-Julian J, Malzbender J. High temperature compressive creep of dense and porous  $\text{Cr}_2\text{AlC}$  in air. *J Eur Ceram Soc.* 2019;39(13):3660–7.
- Radovic M, Barsoum MW. MAX phases: bridging the gap between metals and ceramics. *Am Ceram Soc Bull.* 2013;92(3):20–7.

28. Dash A, Vaßen R, Guillon O, Gonzalez-Julian J. Molten salt shielded synthesis of oxidation prone materials in air. *Nat Mater*. 2019;18(5):465–70.
29. Stournari V, ten Donkelaar SFP, Malzbender J, Beck T, Singheiser L, Bouwmeester HJM. Creep behavior of perovskite-type oxides  $\text{Ba}_{0.5}\text{Sr}_{0.5}(\text{Co}_{0.8}\text{Fe}_{0.2})_{1-x}\text{Zr}_x\text{O}_{3-\delta}$ . *J Eur Ceram Soc*. 2015;35(6):1841–6.
30. Dash A, Sohn YJ, Vaßen R, Guillon O, Gonzalez-Julian J. Synthesis of  $\text{Ti}_3\text{SiC}_2$  MAX phase powder by a molten salt shielded synthesis (MS3) method in air. *J Eur Ceram Soc*. 2019;39(13):3651–9.
31. Low I-M. An overview of parameters controlling the decomposition and degradation of Ti-based Mn+1AX<sub>n</sub> phases. *Materials (Basel)*. 2019;12(3):473.
32. Low IM, Oo Z, Prince KE. Effect of vacuum annealing on the phase stability of  $\text{Ti}_3\text{SiC}_2$ . *J Am Ceram Soc*. 2007;90(8):2610–4.
33. Luo YM, Li SQ, Chen J, Wang RG, Li JQ, Pan W. Effect of composition on properties of alumina/titanium silicon carbide composites. *J Am Ceram Soc*. 2004;85(12):3099–101.
34. Spencer CB. Fiber-reinforced  $\text{Ti}_3\text{SiC}_2$  and  $\text{Ti}_2\text{AlC}$  MAX phase composites. 2010.
35. Li S, Song G, Kwakernaak K, van der Zwaag S, Sloof WG. Multiple crack healing of a  $\text{Ti}_2\text{AlC}$  ceramic. *J Eur Ceram Soc*. 2012;32(8):1813–20.
36. Li S, Xiao L, Song G, Wu X, Sloof WG, van der Zwaag S. Oxidation and crack healing behavior of a fine-grained  $\text{Cr}_2\text{AlC}$  ceramic. *J Am Ceram Soc*. 2013;96(3):892–9.
37. Li S, Li H, Zhou Y, Zhai H. Mechanism for abnormal thermal shock behavior of  $\text{Cr}_2\text{AlC}$ . *J Eur Ceram Soc*. 2014;34(5):1083–8.
38. Pelleg J. Creep in ceramics. In: *Solid mechanics and its applications*. Springer Verlag; 2017, p. 41–61. [https://doi.org/10.1007/978-3-319-50826-9\\_4](https://doi.org/10.1007/978-3-319-50826-9_4)
39. Lee F, Bowman KJ. Texture and anisotropy in silicon nitride. *J Am Ceram Soc*. 1992;75(7):1748–55.
40. Duan X, Jia D, Wu Z, Tian Z, Yang Z, Wang S, et al. Effect of sintering pressure on the texture of hot-press sintered hexagonal boron nitride composite ceramics. *Scr Mater*. 2013;68(2):104–7.
41. Tang K, Wang C, Huang Y, Zan Q, Xu X. A study on the reaction mechanism and growth of  $\text{Ti}_3\text{SiC}_2$  synthesized by hot-pressing. *Mater Sci Eng A*. 2002;328(1-2):206–12.
42. de Arellano-López AR, Domínguez-Rodríguez A, Routbort JL. Microstructural constraints for creep in SiC-whisker-reinforced  $\text{Al}_2\text{O}_3$ . *Acta Mater*. 1998;46(18):6361–73.
43. Cannon WR, Langdon TG. Creep of ceramics. *J Mater Sci*. 1988;23(1):1–20.
44. Barcelo F, Doriot S, Cozzika T, Le Flem M, Béchade J, Radovic M, et al. Electron-backscattered diffraction and transmission electron microscopy study of post-creep  $\text{Ti}_3\text{SiC}_2$ . *J Alloys Compd*. 2009;488(1):181–9.
45. Langdon TG. A unified approach to grain boundary sliding in creep and superplasticity. *Acta Metall Mater*. 1994;42(7):2437–43.
46. Lin H-T, Becher PF. Creep behavior of a SiC-whisker-reinforced alumina. *J Am Ceram Soc*. 1990;73(5):1378–81.
47. Gouriet K, Carrez P, Cordier P, Guitton A, Joulain A, Thilly L, et al. Dislocation modelling in  $\text{Ti}_2\text{AlN}$  MAX phase based on the Peierls-Nabarro model. *Philos Mag*. 2015;95(23):2539–52.
48. Nan C-W. Physics of inhomogeneous inorganic materials. *Prog Mater Sci*. 1993;37(1):1–116.
49. Wilkinson DS, Pompe W. Creep and anelastic recovery of whisker- and platelet-reinforced ceramics. *Acta Mater*. 1998;46(4):1357–69.
50. Radovic M, Barsoum MW, El-Raghy T, Seidensticker J, Wiederhorn S. Tensile properties of  $\text{Ti}_3\text{SiC}_2$  in the 25–1300°C temperature range. *Acta Mater*. 2000;48(2):453–9.
51. Drouelle E, Joulain A, Cormier J, Gauthier-Brunet V, Villechaise P, Dubois S, et al. Deformation mechanisms during high temperature tensile creep of  $\text{Ti}_3\text{AlC}_2$  MAX phase. *J Alloys Compd*. 2017;693:622–30.
52. Farber L, Barsoum MW, Zavaliangos A, El-Raghy T, Levin I. Dislocations and stacking faults in  $\text{Ti}_3\text{SiC}_2$ . *J Am Ceram Soc*. 2005;81(6):1677–81.

## SUPPORTING INFORMATION

Additional supporting information may be found online in the Supporting Information section.

**How to cite this article:** Dash A, Malzbender J, Dash K, et al. Compressive creep of SiC whisker/ $\text{Ti}_3\text{SiC}_2$  composites at high temperature in air. *J Am Ceram Soc*. 2020;103:5952–5965. <https://doi.org/10.1111/jace.17323>